Structural basis of transfer between lipoproteins by cholesteryl ester transfer protein

Lei Zhang[1-3,11], Feng Yan[2,11], Shengli Zhang[3], Dongsheng Lei[3], M Arthur Charles[2], Giorgio Cavigiolio[4], Michael Oda[4], Ronald M Krauss[4], Karl H Weisgraber[5], Kerry-Anne Rye[6-8], Henry J Pownall[9], Xiayang Qiu[10] & Gang Ren[1-3]*

Human cholesteryl ester transfer protein (CETP) mediates the net transfer of cholesteryl ester mass from atheroprotective high-density lipoproteins to atherogenic low-density lipoproteins by an unknown mechanism. Delineating this mechanism would be an important step toward the rational design of new CETP inhibitors for treating cardiovascular diseases. Using EM, single-particle image processing and molecular dynamics simulation, we discovered that CETP bridges a ternary complex with its N-terminal β-barrel domain penetrating into high-density lipoproteins and its C-terminal domain interacting with low-density lipoprotein or very-low-density lipoprotein. In our mechanistic model, the CETP lipoprotein-interacting regions, which are highly mobile, form pores that connect to a hydrophobic central cavity, thereby forming a tunnel for transfer of neutral lipids from donor to acceptor lipoproteins. These new insights into CETP transfer provide a molecular basis for analyzing mechanisms for CETP inhibition.

CETP mediates the transfer of neutral lipids, including cholesteryl esters and triglycerides, between high-density lipoproteins (HDL), low-density lipoproteins (LDL) and very-low-density lipoproteins (VLDL)[1]. Elevated LDL cholesterol (LDL-C) level and/or low HDL cholesterol (HDL-C) level in human plasma are major risk factors for cardiovascular disease[2,3]. As increased CETP level can reduce HDL-C concentration[4] and CETP deficiency is associated with elevated HDL-C[5,6], CETP inhibitors, including torcetrapib, anacetrapib and dalcetrapib, have been investigated in clinical trials for treating cardiovascular disease[7–9]. Despite the intense clinical interest in CETP inhibition, little is known concerning the molecular mechanisms of CETP-mediated lipid transfer among lipoproteins or even how CETP interacts with lipoproteins.

CETP is a hydrophobic glycoprotein of 476 amino acids (~53 kDa before post-translational modification). Its crystal structure reveals a banana-shaped molecule with N- and C-terminal β-barrel domains, a central β-sheet and an ~60-Å-long hydrophobic central cavity. The cavity, which can accommodate two cholesteryl ester molecules, communicates with two pores near the central β-sheet domain. These pores, which are occupied by two phospholipid molecules, could be gates for the interaction of the central cavity with the aqueous environment or lipoproteins[10].

Three CETP neutral lipid transfer hypotheses were proposed in 1980, 1982 and 1993, respectively: (i) a shuttle mechanism that involves CETP collecting cholesteryl esters from one lipoprotein and delivering them through the aqueous phase to another lipoprotein[11]; (ii) a tunnel mechanism in which CETP bridges two lipoproteins to form a ternary complex, with lipids flowing from the donor to acceptor lipoprotein through the CETP molecule[12]; and (iii) a modified tunnel mechanism implicating a CETP dimer[13].

One difficulty in investigating CETP mechanisms using structural methods is that interaction with CETP can alter the size, shape and composition of lipoproteins, especially HDL[14–16]. We validated an optimized negative-staining (OpNS) EM protocol[14,17] in which flash fixation of lipoprotein particles preserves a near native-state conformation for direct visualization of individual macromolecular particles. We applied this protocol to study the mechanisms by which CETP interacts with spherical HDL, LDL and VLDL. Three-dimensional reconstructions of CETP, free and HDL bound, were obtained by single-particle techniques. In addition, we used inhibitory CETP-specific antibodies to identify the regions of CETP that interact with HDL and LDL. Finally, molecular dynamics simulation was used to assess the molecular mobility of CETP and predict the most likely conformational changes that are associated with lipid transfer.

RESULTS

Structure of CETP using EM

Conventional cryo-EM is often the method of choice for studies of protein structure under physiological conditions because it avoids the potential artifacts induced by fixatives and stains[17]. Still, cryo-EM studies of CETP are challenging; small molecules (<200 kDa) are difficult to image or reconstruct by the cryo-EM single-particle approach because of low contrast[18]. Thus, we studied human recombinant CETP by using OpNS[14,17] and a cryo–positive-staining EM (cryo-PS-EM) protocol.

Our OpNS protocol, refined from the conventional negative-staining protocol, eliminates rouleaux artifacts of lipoprotein particles and was statistically validated as a way to determine lipoprotein particle shapes and sizes[14,17]. The cryo-PS-EM protocol was developed by combining our OpNS[14,17] and conventional cryo-EM protocols[19–21]. Instead of air-drying the sample in the last step of the negative-staining protocol, we flash-froze the sample in liquid nitrogen. As the cryo-EM image of a
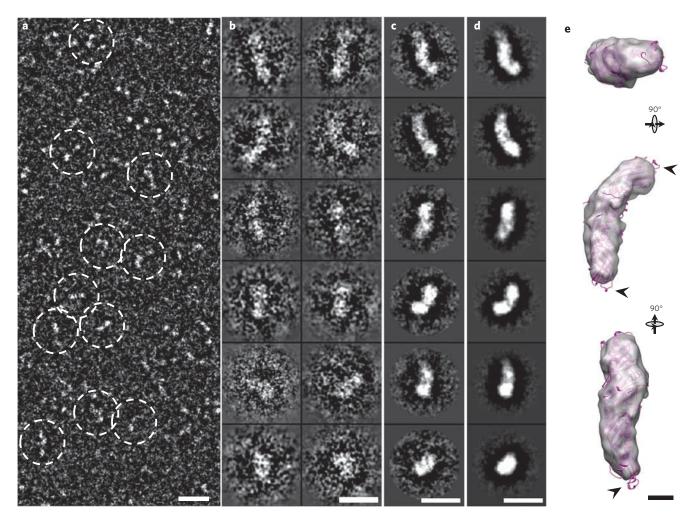
Figure 1 | Three-dimensional reconstruction of CETP by cryo-PS-EM. (**a**) Survey view (reversed contrast) of CETP molecule alone (dashed circles). (**b–d**) Twelve representative views of selected and windowed raw particles of CETP (**b**) and their class averages (**c**) are compared with corresponding views of the projections of the three-dimensional reconstruction (**d**). (**e**) The crystal structure of CETP (purple) inserted into the three-dimensional EM density map (~13-Å resolution) demonstrates a near-perfect match to the density map in shape and size, except for the distal portions of the N- and C-terminal β-barrel domains, segments of which protrude (arrowheads) from the density envelope. Scale bars: **a–d**, 100 Å; **e**, 20 Å.

particle has reversed contrast compared to that produced using the reported cryo-NS protocol[22] but has image contrast consistent with that of a conventional cryo-EM image, we call it the cryo-PS-EM protocol.

We compared the particle shape and size in images of CETP with that in the CETP crystal structure (Protein Data Bank code 2OBD[10]). Survey-OpNS-EM micrographs and selected particle views revealed the expected banana-shaped CETP with dimensions of 125 Å × 30 Å (**Supplementary Results**, **Supplementary Fig. 1a,b**). When the CETP crystal structure is overlaid on a reference-free class average of OpNS-EM images, a near-perfect match in shape and size is found (**Supplementary Fig. 1c,d**), and it is notable that even the concave surface, C-terminal end (more globular) and N-terminal end (more tapered) of CETP are readily distinguished (**Supplementary Fig. 1d**). These studies validate direct OpNS-EM as a way to visualize the structure of CETP in other settings in which it associates with various lipoproteins.

Survey cryo-PS-EM micrographs (**Fig. 1a** and **Supplementary Fig. 2a**) and selected particle views (**Fig. 1b** and **Supplementary Fig. 2b**) also showed the banana-shaped CETP with a shape and dimensions similar to those observed in micrographs from OpNS-EM (**Supplementary Fig. 1**). These cryo-PS-EM images of CETP were also used to reconstruct a three-dimensional density

map of CETP using the single-particle reconstruction method[21]. Again, the class averages and the projections of the reconstructed three-dimensional density map show a banana-shaped density (~125 Å × 30 Å) with a shape and size similar to those of the crystal structure (**Fig. 1c–e** and **Supplementary Fig. 2c–g**) at ~13-Å resolution (**Supplementary Fig. 3**); once again, we observed a near-perfect fit of the crystal structure into the envelope of the three-dimensional density map, suggesting that the density map can be used to determine the CETP concave surface orientation (**Fig. 1e** and **Supplementary Fig. 2f,g**), with the C-terminal (more globular end) and N-terminal (more tapered end) domains at the ends of the long CETP axis. Some hydrophobic loops were observed outside the CETP envelope at the distal portions of the N- and C-terminal β-barrel domains, suggesting that these regions have structural flexibility (arrows in **Fig. 1e**).

Notably, some raw particle images (~50%) show substantial structural detail (**Fig. 2** and **Supplementary Fig. 4**). For example, at specific viewing orientations, a manual noise-decreasing procedure performed on the raw particle images near the particle boundary (**Fig. 2** and **Supplementary Fig. 4**) revealed that the particle outer features are remarkably similar to the crystal structure (**Fig. 2** and **Supplementary Fig. 4**). Thus, the particle internal features show parallel fringes that are well
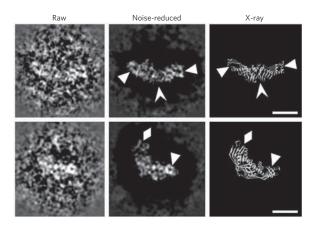
343

Figure 2 | High-resolution CETP images by cryo-PS-EM. Two selected high-resolution and raw particle images of CETP (contrast reversed, left column) were manually noise reduced around the raw particle images' edges for easy visualization (middle column). The latter images can be compared with those of the X-ray crystal structure's main chain at a similar orientation (right column). The high-resolution raw image areas show detailed structural features of CETP. These particles have very similar features to the crystal structure; for example, the small circular holes near both distal ends can be visualized in the noise-reduced images (triangles in both rows); further, the striations in the C-terminal domains of the images match the β-sheets of the crystal structure (arrowheads in top row), and loops protruding from the C-terminal end of the CETP images are similar to the crystal structure (diamonds in bottom row). Scale bars, 50 Å.

matched to the β-sheet strands within the C-terminal β-barrel domain of the crystal structure as well as to end loops and holes (**Fig. 2** and **Supplementary Fig. 4**). Imaging of internal structural features was achieved by using EM imaging conditions of near-Scherzer focus (~0.1 μm) and higher doses (~60–70 e⁻ Å⁻²) rather than conventional cryo-EM conditions such as high defocus (~2–3 μm) and low doses (~20 e⁻ Å⁻²). These high-resolution images show that CETP can be visualized directly by this cryo-PS-EM protocol, confirming our findings above using OpNS-EM. Moreover, the cryo-PS-EM images show that the staining reagent, uranyl formate, penetrates the molecular surface, challenging the conventional view that staining can visualize only the outer surface structure[23]. The mechanism of how uranyl formate penetrates the molecular surface is unknown. One possibility is that the uranyl cation binds available protein carboxyl groups, and thus the surrounding vitreous ice is of lower density than the staining of the protein and uranyl groups, thereby acting as a positive.

Even though we show that unexpectedly detailed secondary structural elements can be observed with the cryo-PS-EM method in individual images, the final three-dimensional reconstruction did not show the high-resolution details shown in our cryo-PS-EM two-dimensional images. This may be due to (i) the flexibility of the entire CETP molecule, (ii) variation of two-dimensional image quality in that only ~50% of these images contain more or less high-resolution structural details (the loss of detail may be due to the variation of the coated stains, particle orientation, ice thickness or a combination of the three) and/or (iii) the limited capability of the two-dimensional class-average program used for three-dimensional reconstructions. Therefore, the high-resolution details were quickly smeared after the class-average process. Because the three-dimensional reconstructions from cryo-PS-EM images provided no additional insights beyond those resulting from our OpNS-EM images and the cryo-PS-EM is a time-consuming procedure, the simpler, OpNS-EM protocol was used for the remainder of experiments (described below).

Structure of the HDL–CETP complex by electron microscopy

To determine how CETP interacts with HDL, we incubated CETP with HDL at CETP:HDL molar ratios between 0.5:1 and 5:1 and examined the products using the OpNS-EM protocol. We observed spherical HDL particles (diameter ~85–110 Å) with a single protruding feature that was not seen in the absence of CETP, and we concluded that the protrusion is CETP that is part of a binary complex (**Fig. 3a,b** and **Supplementary Figs. 5** and **6**); less than ~10% of HDL–CETP complexes have two or more protruding CETP molecules that often share the same half of the HDL surface (**Supplementary Fig. 7**). No CETP molecule that was configured with its concave surface adjacent to the convex surface of HDL or that bridged two HDL particles to form a ternary complex was observed, suggesting that CETP has HDL binding directionality. As the total number of CETP molecules bound to HDL can be greater than the total number of apolipoprotein A-I (apoA-I) molecules in HDL, apoA-I is not likely to be involved in CETP binding, supporting the previous model based on protein-free vesicles known as liposomes[24,25].

In binary complexes, the CETP N-terminal domain (more tapered end) appears to interact with HDL. Measurement of more than 100 binary complexes revealed a CETP width of ~30 Å, whereas the length protruding from the HDL surface was ~77 ± 10 Å (**Supplementary Fig. 5b**), which is notably shorter than the length of CETP alone (~125 Å). This observation suggests that the remainder of CETP (~48 ± 10 Å) penetrates through the HDL surface or, alternatively, partitions tangentially into the HDL lipid surface and that the free-end portion of CETP seems more likely to be the globular end of CETP (C-terminal domain, **Supplementary Fig. 5c**). This measurement provoked the hypothesis that the distal CETP N-terminal end penetrates into or through the phospholipid portion of the HDL surface under physiological conditions. Preliminary studies of native human HDL, prepared by immunoabsorption, and liposomes show similar CETP-macromolecule relationships, as shown in **Figure 3a,b** and **Supplementary Figures 5, 6a,b** and **7**.

CETP penetration of HDL revealed by 3D reconstructions

To study the CETP interaction with HDL in more detail, we generated a three-dimensional density map of the HDL–CETP complex from OpNS-EM images (**Fig. 3a–e** and **Supplementary Fig. 6a–f**) with the single-particle reconstruction protocol used for LDL three-dimensional reconstructions[21]. To obtain higher-resolution reconstruction of the HDL–CETP complex, we computationally selected a homogenous population of ~6,600 particle images from an original pool of ~20,000 images using the same batch program that was used for LDL reconstruction[21]. The convergent reconstruction from this subpopulation of particle images (**Fig. 3b,c** and **Supplementary Fig. 6b,c**) provides a statistically defined and robust density map showing the most prominent and reliable structural features of the HDL–CETP complex (**Fig. 3d** and **Supplementary Fig. 6d,e**).

A 14-Å-resolution (**Supplementary Fig. 3**) three-dimensional map reveals a quasispherical HDL (~100 Å × 110 Å × 115 Å) attached to the end of a banana-shaped CETP (~80-Å free end × 45-Å penetrating end × 25-Å width) at a contour level corresponding to the molecular volume of the complex (**Fig. 3e** and **Supplementary Fig. 6f**). This spherical HDL contains an 18- to 27-Å high-density outer shell and a low-density core (diameter ~55 Å; **Supplementary Fig. 6g**), whereas the banana-shaped CETP portion has a concave surface protruding ~45° from the HDL surface. The curvature of the banana-shaped portion is similar to that observed after EM reconstruction of CETP alone (**Fig. 1e**).

To determine the CETP orientation, we inserted the CETP crystal structure into the banana-shaped portion of the binary HDL–CETP complex density envelope (**Fig. 3f**) using two structural analysis
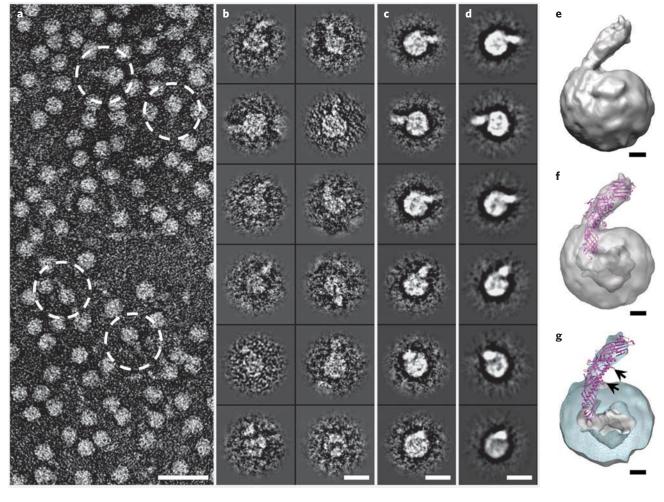
Figure 3 | Three-dimensional reconstruction of HDL–CETP complex by OpNS-EM. (**a**) Survey view of the negative-stained EM structure of HDL–CETP complexes (dashed circles). (**b**–**d**) Twelve representative views of selected and windowed individual raw particles of HDL–CETP complexes (**b**) and their corresponding class averages (**c**) are compared with the same views of the reconstructed projections (**d**). (**e**) The three-dimensional density map (~14-Å resolution, reconstructed from 6,607 homogenous particle images) shows a binary complex in which the banana-shaped CETP is attached to the HDL surface at a ~45° angle. (**f,g**) Inserting the CETP crystal structure into the EM density map of an HDL–CETP complex shows the N-terminal β-barrel domain of CETP penetrating the outer shell of HDL and its distal end in the low-density core in transparency (**f**) and cut-away surface view (**g**). The cut-away surface view (cyan) in **g** shows the HDL portion containing a high-density outer shell (~18–27 Å thick) and a low-density cavity (~55 Å in diameter). The black arrows in **g** point to two phospholipid-binding pores, one of which is adjacent (~15 Å) to the HDL surface, whereas the other is further away, indicating that the phospholipid-binding pores of CETP do not interact directly with the HDL core. Scale bars: **a**, 300 Å; **b**–**d**, 100 Å; **e**–**g**, 20 Å.

methods in Chimera[26]. Using the atom-in-map method[26], we fit the CETP C-terminal domain of the crystal structure into the free-end portion of the HDL–CETP density map, producing an average map value fit of 5.373. In contrast, inserting the N-terminal domain into the free end gave a lower value, 5.232. Using the map-in-map method[26], a 14-Å-resolution density map generated from the crystal structure was inserted into the free end to calculate the correlation values, which were $r = 0.9480$ and $r = 0.8972$ for the C- and N-terminal CETP domains, respectively. Both analyses confirm the interaction of the N-terminal domain with HDL. Inserting the CETP crystal structure into the HDL–CETP envelope shows that 48 Å of the tapered N-terminal end of CETP penetrates the HDL surface (**Fig. 3f**), reaching the cholesteryl ester–rich, low-density core (**Fig. 3g**).

Inserting the CETP crystal structure into the binary complex also shows that the phospholipid-binding pores of CETP, which are thought to be involved in lipid transfer, do not interact directly with the cholesteryl ester–rich HDL core. One phospholipid-binding pore is adjacent (~15 Å) to the HDL surface, whereas the other is further away (arrows in **Fig. 3g**), suggesting that the pore adjacent

to the HDL surface may be a neutral lipid pore for cholesteryl ester transfer through the HDL surface. Alternatively, the portion of the N-terminal domain that penetrates into the cholesteryl ester core may generate another, perhaps more efficient, pore for cholesteryl ester transfer.

CETP domains interact with HDL and LDL or VLDL
CETP was incubated separately with LDL and VLDL and was examined by the OpNS-EM protocol. Spherical LDL (diameter ~200–270 Å) and VLDL (diameter ~370–570 Å) particles were observed with a single CETP protruding from their surfaces as part of a binary complex (**Fig. 4a,b** and **Supplementary Fig. 8**). Although we observed neither LDL–CETP complexes with two protruding CETP molecules nor two LDLs or VLDLs bridged by one CETP, we did observe occasional VLDL particles with more than one attached CETP molecule. The ability of multiple CETP to attach to one VLDL particle may be due to different surface properties induced by differing apolipoprotein compositions and lipid surface curvatures and areas. Measurements of >100 of these binary complexes revealed that the free-end width of CETP is ~30 Å, similar to
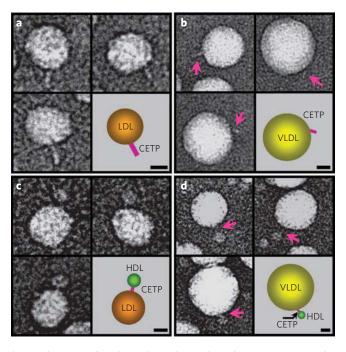
Figure 4 | Structural conformations of CETP bound to LDL or VLDL and CETP interactions between lipoproteins by OpNS-EM. (**a**) Linear- or banana-shaped CETPs (~100 ± 10 Å long) associated with the surfaces of LDL (diameter ~200–270 Å) particles. (**b**) Linear-shaped CETPs (~105 ± 10 Å long, pink arrows) protruding from the surfaces of VLDL particles (diameter ~370–570 Å). (**c**) Linear-shaped CETPs (~25–55 Å long) bridge HDL particles (diameter ~85–110 Å) to LDL particles, forming ternary complexes. (**d**) VLDL particles connected to HDL particles via linear-shaped CETPs (~35–65 Å long, pink arrows), forming ternary complexes similar to those formed with LDL. The schematic on the bottom right of each panel represents the corresponding complex on the bottom left of each panel. Scale bars, 100 Å.

that observed for the HDL–CETP complexes. The free-end lengths on LDL and VLDL are ~100 ± 10 Å and ~105 ± 10 Å, respectively, and are shorter than the length of CETP alone (~125 Å), suggesting that the hidden portions of CETP penetrating the LDL and VLDL surfaces are ~25 ± 10 Å and ~20 ± 10 Å, respectively (**Fig. 4a,b** and **Supplementary Fig. 8**).

An antibody can be used as a landmark to define the orientation of protein binding by EM[27,28]. A domain-specific polyclonal antibody to CETP, H300, whose epitopes are within a region containing the entire C-terminal β-barrel domain and part of the central β-sheet (residues 194–493), was used to identify the parts of CETP that penetrate lipoproteins. The OpNS-EM micrographs of the HDL–CETP complex show a characteristic 'Y'-shaped density, usually near the free end of CETP (**Supplementary Fig. 9**). In contrast, LDL–CETP–H300 complexes were rarely seen in the micrographs obtained from the incubations of H300 with LDL and CETP (**Supplementary Fig. 10**), suggesting that the CETP epitopes to H300 are buried within the LDL particle. Moreover, the percentage of binary complexes (LDL–CETP) formed in the presence of H300 was also lower than that without H300 (<15% versus ~38%), suggesting that H300 inhibits CETP-LDL interaction. These experiments are consistent with the N-terminal domain of CETP interacting with HDL while the C-terminal domain preferentially interacts with LDL. These data are also consistent with the fitting of the crystal structure into the three-dimensional density map and two-dimensional images of the HDL–CETP complex and with the dimensions calculated from the CETP pores to the HDL surface.

CETP bridges HDL to LDL or VLDL to form ternary complexes

After co-incubation of CETP, HDL and LDL, the OpNS-EM micrographs showed ~25% of LDL particles connecting to HDL particles by a ~25- to 55-Å-long CETP bridge (**Fig. 4c** and **Supplementary Fig. 11a–c**). The length of the bridge was much shorter than the length of CETP alone (~125 Å), indicating that CETP penetrates into one or both lipoprotein surfaces or cores to form the ternary complex. When co-incubation was repeated with VLDL, ~30% of the VLDL particles were connected to HDL particles by CETP bridges (length ~35–65 Å; **Fig. 4d** and **Supplementary Fig. 11d–f**). Unlike LDL, ~30% of the VLDL complexes were bound to more than one HDL–CETP complex, most likely because they contain more protein, which provides more 'binding sites'; bridges between lipoproteins of the same class were not observed, further supporting the hypothesis that HDL and LDL or VLDL bind different CETP domains. The coexistence of ternary complexes of HDL–CETP–LDL and HDL–CETP–VLDL and lipid transfer (shown in **Fig. 5** and **Supplementary Fig. 12**) are consistent with the mechanistic model of cholesteryl ester transfer through a tunnel within CETP. These observations do not totally exclude the shuttle mechanism, as the ternary complexes coexisted with the binary complexes HDL–CETP and LDL–CETP. However, the tunnel mechanism seems more plausible because it is directly supported by the observation that CETP bridges HDL to LDL or VLDL to form a ternary complex.

CETP reaction mechanism

CETP with HDL, LDL or both was incubated with or without the CETP-specific polyclonal antibodies H300 and N13 at physiological temperatures for up to 48 h, during which HDL size was measured using the OpNS-EM. These experiments (**Fig. 5**, **Supplementary Fig. 12** and **Supplementary Table 1**; details shown in **Supplementary Results**) do not support the shuttle mechanism in which CETP dissociates from the HDL surface after it has removed the maximum amount of cholesteryl ester from the HDL core.

Although the results do not favor the shuttle mechanism for CETP-mediated transfer of neutral lipids between HDL and LDL, they do not exclude the possibility that CETP shuttles neutral lipids between HDL particles themselves (**Supplementary Results**).
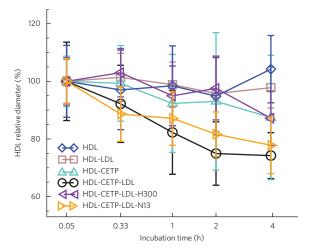

Figure 5 | Analysis of HDL size change during incubation with CETP. Samples were collected and viewed by OpNS-EM. A total of ~500 HDL particles for each incubation condition were selected from EM micrographs for quantitative size analysis. The geometric sizes of particles were calculated (**Supplementary Methods**) and expressed as the mean ± s.d. Quantifying the size of HDL particles for HDL alone (blue) and for HDL-LDL (brown) and HDL-CETP (cyan) mixtures shows no substantial size changes during the incubation time except for in the ternary HDL-CETP-LDL mixture (black). The diameters of HDL particles following incubations with LDL and CETP in the presence of antibodies H300 (purple) and N13 (gold) are also shown.

CETP hydrophobic central cavity

A series of hydrophobic cavities exist in the crystal structure of CETP. The occurrence of a hydrophobic pore within the N-terminal distal portion of CETP and a hydrophobic tunnel connecting the distal portions of the N- and C-terminal regions would support the tunnel mechanism. Therefore, the van der Waals surface of the CETP crystal structure was visualized as a colored surface according to its hydrophobicity (**Fig. 6a**). Longitudinal cross-sections of the surface density of CETP from the N-terminal β-barrel domain to the C-terminal β-barrel domain reveal a 60-Å-long hydrophobic central cavity traversing the central β-sheet domain, as reported previously[10]. To our surprise, a series of additional small, hollow, isolated hydrophobic cavities (diameter >5 Å) are present along the central axis of both β-barrel domains, lateral to the central β-sheet and the previously reported central cavity (**Fig. 6b**). The occurrence of unconnected cavities aligned linearly over ~105 Å, including both barrel domains and the ~60-Å central cavities, suggests that the crystal structure of CETP might show a 'closed' state with respect to cholesteryl ester transfer. Connecting the central cavity with these isolated lateral cavities could, if the protein is in an 'activated' state, connect all of the cavities to form a continuous tunnel between the distal portions of the N- and C-terminal domains for cholesteryl ester transfer. At this point, the continuous hydrophobic tunnel is hypothetical, and CETP's activated state is speculative and requires confirmation from X-ray crystallography.

Molecular dynamics simulations predict a continuous central tunnel within CETP. Interaction of CETP with the surface monolayer and the core of a lipoprotein would have to trigger a conformational change at the distal portions of the β-barrel domains to open the continuous tunnel that accommodates entry of a cholesteryl ester into the central cavity and its exit from the opposite end. This would require high flexibility within the distal portions of the β-barrel domains. Because the N- and C-terminal β-barrel domains (i) penetrate the HDL, LDL and VLDL surfaces; (ii) have distal ends rich in hydrophobic amino acids; (iii) are in close proximity to the lipoprotein core; and (iv) have structurally flexible regions as suggested by the hydrophobic loops outside the CETP EM envelope at both distal portions of the β-barrel domains, we hypothesized that the ends of both the N- and C-terminal β-barrel domains undergo conformational changes that initiate cholesteryl ester transfer. To test this hypothesis, we analyzed the regional mobility of CETP and predicted the molecular motions within CETP using two molecular dynamics simulation methods. The nanoscale molecular dynamics method[29] showed that the residues containing the top 30% of fluctuations are mostly on both ends of the CETP β-barrel domains and on the α-helix X (**Supplementary Fig. 13a–c**). The greatest structural fluctuation occurs near the distal end of the N-terminal β-barrel domain, which is consistent with the distal portions outside the EM envelope depicted in **Figure 1e**. Similar events most likely occur at the C terminus as well.

To investigate whether the flexibility of the domains contributes to the formation of a continuous tunnel between unconnected hydrophobic cavities, we analyzed the vibrational motions of CETP under 20 interrupting modes using the anisotropic network model, which predicts large-scale fluctuations[30,31]. This analysis showed that the ends of the β-barrel domains are flexible (**Supplementary Fig. 13d**). Remarkably, a ~15° twist along the long axis of CETP (**Supplementary Fig. 13d**) is associated with a ~10° tilt of the β-barrel strands (**Supplementary Fig. 13e**). Torsional analysis shows slight widening of the tunnel (~5 Å); thus, the central cavity connects with all of the small hydrophobic cavities to form a ~120-Å tunnel that is ~5–15 Å wide (**Supplementary Fig. 13f–h**). These analyses are consistent with the hypothesis that the ends of CETP β-barrel domains are subject to low-energy flexing that may gate cholesteryl ester entry into the central tunnel, which must open
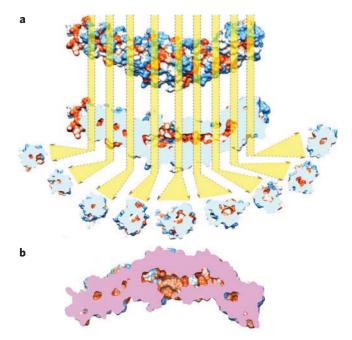
Figure 6 | Analyses of the crystal structure of CETP. (**a**) The CETP crystal structure is shown according to its van der Waals surface and is colored by its hydrophobicity (ranging from royal blue for the most hydrophilic to orange-red for the most hydrophobic). Longitudinal cut-away cross-sections show hydrophobic cavities (orange) from the center of the N-terminal β-barrel domain to the center of the C-terminal β-barrel domain. The distal portions of both β-barrels of CETP appear to be sealed. The cavities were aligned along the center of each domain, potentially reflecting the cholesteryl ester transfer pathway. The longest dimension of the pathway is about ~105 Å. (**b**) The cut-away surface view of CETP. The side openings near the center of the molecule are the phospholipid-binding pores. Pink regions show the cross surface between the cutting plane and the CETP molecule.

at both ends for cholesteryl ester transfer. The tunnel is hydrophobic and connects the distal ends of the β-barrel domains to form a continuous central tunnel that mediates cholesteryl ester transfer.

DISCUSSION

On the basis of the present findings, we propose a model (**Fig. 7**) in which both CETP terminal ends, including the N-terminal domain's hydrophobic mini helix and strands and the C-terminal domain's hydrophobic Ω_2 strand, penetrate surface sites on lipoproteins to access the surface, central core or both (**Fig. 7**), similar to that for the association of exchangeable apolipoproteins to lipoprotein surfaces[32,33]. These interactions induce torsion of the two distal domains of CETP, which is the key to opening the tunnel for neutral lipid transfer. We also propose that cholesteryl ester migrates from HDL, which resides in a high-energy kinetic trap[34,35], to LDL or VLDL through a hydrophobic tunnel structure (**Fig. 7**). The thermodynamic forces that drive cholesteryl ester transfer from HDL are (i) differential cholesteryl ester concentrations in donor and acceptor particles, (ii) changes in hydrophobicity along the central cavity favoring cholesteryl ester N- to C-terminus transfer and (iii) different internal densities, for example, LDL (less dense cholesteryl ester regions)[21] or VLDL (triglyceride-rich environment)[35]. We further speculate that phospholipid pores could permit phospholipid movement out of the surface layer of HDL to accommodate an increase in surface curvature and into the surface of the acceptor lipoprotein (for example, LDL and VLDL) to accommodate a decrease in surface curvature. In step 4 in **Figure 7**, the ternary complex dissociates. Our model is consistent with mutagenesis data[36] showing that substitution of polar amino acids for hydrophobic ones is associated with
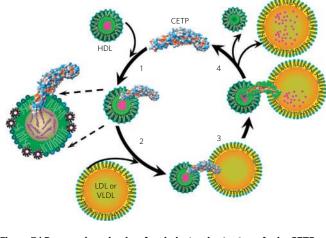
Figure 7 | Proposed mechanism for cholesteryl ester transfer by CETP.
The N-terminal β-barrel domain of CETP initially penetrates the HDL surface, and the distal end of the domain interacts with the cholesteryl ester core of HDL (1). Upon interaction of the C-terminal β-barrel domain with LDL or VLDL (2), molecular forces introduced by the lipoproteins at either end of CETP cause twisting of the β-barrel domains and pore formation at the distal ends of the N- and C-terminal domains. These pores connect with the hydrophobic, continuous and central cavities of CETP to form a tunnel (3) that serves as a conduit, resulting in a transfer of cholesteryl esters to LDL or VLDL and a reduction in HDL size (4).

less neutral lipid transfer, that mutation of the N-terminal phospholipid pore decreases neutral lipid transfer by interfering with tunnel hydrophobicity and that a six-amino-acid deletion mutation of the small amphipathic α-helix X of C-terminal origin decreases maximal neutral lipid transport but not initial CETP binding to HDL, suggesting that α-helix X is important for function.

In summary, CETP was directly visualized as a banana-shaped asymmetric molecule with a tapered N-terminal end and a globular C-terminal end; according to our observations, the N-terminal end penetrates into HDL. There are near-perfect fits of overlays and insertion of the crystal structure into two- and three-dimensional structures. The dimensions of the portions of CETP that penetrate HDL and LDL or VLDL are distinct, and their subtraction from the total length of CETP approximates the length of the bridge observed between HDL and LDL or VLDL. Additionally, the C terminus–specific H300 antibody associates with the free end of CETP protruding from HDL, and H300 blocks formation of a LDL–CETP binary complex but not that of a HDL–CETP complex. The appearance of HDL–CETP–LDL ternary complexes strongly supports the tunnel mechanism for neutral cholesteryl ester transfer. We observed CETP terminal ends bridging lipoproteins; cholesteryl ester transfer occurs in the presence of the ternary complexes; the H300 antibody inhibits ternary complex formation and transfer activity; even after long incubations, the percentage of HDL–CETP complexes shows no observed decrease over time; and molecular simulations suggest that a hydrophobic tunnel spans the length of CETP. Our proposed CETP structure reveals the portions that are involved in mediating cholesteryl ester transfer and could be targeted by new classes of CETP inhibitors.

METHODS

Protein isolation and purification. Recombinant human CETP (~53 kDa before post-translational modifications) and lipoprotein were purified as described in detail in **Supplementary Methods**.

CETP–lipoprotein complex formation. CETP–HDL, HDL–CETP–LDL and HDL–CETP–VLDL complexes were prepared as described in detail in **Supplementary Methods**.

Negative-staining EM specimen preparation by the OpNS protocol. Specimens were prepared for EM by the OpNS protocol as described[14,17]. In brief, CETP (final concentration 0.93 mg ml^{-1} (17.5 μM)) and HDL–CETP (final concentration 0.93 mg ml^{-1}) complexes were diluted to 0.005 mg ml^{-1} with Dulbecco's phosphate-buffered saline (DPBS: 2.7 mM KCl, 1.46 mM KH$_2$PO$_4$, 136.9 mM NaCl and 8.1 mM Na$_2$HPO$_4$; Invitrogen) buffer. An aliquot (~3 μl) was placed on a thin, carbon-coated 300-mesh copper grid (Cu-300CN, Pacific Grid-Tech) that had been glow discharged. After ~1 min, excess solution was blotted with filter paper. The grid was washed by briefly touching the surface of the grid with a drop (~30 μl) of distilled water on parafilm and blotting dry with filter paper. This touching and blotting step was performed three times, each time with a clean drop of distilled water. Three drops of 1% (w/v) uranyl formate negative stain (Pacific Grid-Tech) on parafilm were then applied successively, and excess stain was removed by blotting in the same fashion. The grid was allowed to remain in contact with the last drop of stain with the sample side down for 1–3 min in the dark before removal of excess stain and was air dried at ~22 °C (refs. 14,17). Because uranyl formate solutions are light sensitive and unstable, the newly prepared solution was aliquoted and stored in the dark at –80 °C. Just before use, each aliquot was thawed in a water bath in the dark and then filtered (0.02-μm filter). The filter syringe was wrapped with aluminum foil to protect the uranyl formate solution from light. The same protocol was used to prepare other binary and ternary complexes. The lipoprotein particle sizes and shapes obtained from our OpNS protocol have <5% difference from those obtained from the frozen-hydrated native state by cryo-EM of apolipoprotein E4 (apoE4) HDL particles[14,17]. In the conventional negative-staining protocol[17], lipoprotein particles result in the generation of stain-induced structural artifacts, including rouleaux, whereas with our OpNS protocol, rouleaux artifacts are reduced by using uranyl formate instead of phosphotungstic acid at low salt conditions[14,17].

Cryo-PS-EM specimen preparation and EM data collection. CETP specimens were also prepared by a cryo-PS-EM method. In detail, CETP (final concentration 0.93 mg ml^{-1}) was diluted to 0.005 mg ml^{-1} with DPBS buffer, and an aliquot (~3 μl) was applied to a glow-discharged holey thin-carbon-film–coated 300-mesh copper grid (Cu-300HN, Pacific Grid-Tech) for 1 min. The grid was washed with deionized water droplets, and 1% (w/v) uranyl formate (Pacific Grid-Tech) was applied as in the OpNS protocol. Instead of air-drying in the last step, the samples were flash-frozen in liquid ethane under conditions of 100% humidity and 4 °C with a FEI Vitrobot rapid-plunging device after being blotted with filter paper (#595, Schleicher & Schuell) from both sides for 2 s. The frozen-hydrated specimens were transferred to liquid nitrogen for storage. Cryo-PS-EM micrographs were acquired at –180 °C on a Gatan UltraScan 4K × 4K CCD camera by a FEI Tecnai 20 transmission electron microscope (Philips Electron Optics–FEI) or a Zeiss Libra 120 Plus transmission electron microscope (Carl Zeiss NTS) with 20-eV in-column energy filter operating at 200 kV or 120 kV at ×80,000 magnification and low-electron-dose conditions under Scherzer focus, whereas NS-EM micrographs were acquired at ~20 °C with the same CCD camera and magnification but under a defocus of 0.1–0.7 μm. Each pixel of the micrographs corresponded to 1.41 Å or 1.48 Å in the specimens.

The contrast of the image obtained from this cryo-PS method is inverted compared to that from the cryo-NS method reported previously[22]. In the prior cryo-NS method, an exceptionally high concentration of negative stain, 16% (w/v) ammonium molybdate, was used to maintain the negative image contrast from cryo-NS specimens[22], whereas 1% uranyl formate was used in this paper.

Three-dimensional reconstruction of the HDL–CETP complex. Images were processed with FREALIGN, EMAN and SPIDER software packages[37–39]. The defocus and stigmatism of each micrograph were determined by fitting the contrast transfer function (CTF) parameters with its power spectrum by using *ctffind3* in the FREALIGN software package[37]. Micrographs with poor correlation of phase residuals, large stigmatism (>0.1 μm) or distinguishable drift were excluded. The phase of each micrograph was corrected by a Wiener filter with the SPIDER software package[38]. Only isolated particles from the NS-EM images were initially selected and windowed as 256 × 256 pixel images (~360 Å × 360 Å at the specimen) using the *boxer* program in EMAN[39]. For three-dimensional reconstruction and refinement, we used the same program as that used for further selecting lipoprotein particles with a homogeneous size, which we term a 'computational size-exclusion gel-filtration' algorithm[21]. Using this method, ~38% of the particles in total were used for three-dimensional reconstruction, from which ~317 class averages were generated by reference-free class averages computed using *refind2d.py* in EMAN[39]. To prevent bias from a starting model, we used a featureless, smooth, solid cylinder (length ~75 Å, diameter ~35 Å) perpendicularly attached to a featureless, solid Gaussian globule (diameter 120 Å × 100 Å × 80 Å) as an initial starting model. This model was generated on the basis of typical features in reference class averages[40]. For the first four rounds of refinement, only very-low-resolution particle information was used (below the first CTF 0 in reciprocal space). Iterative refinement proceeded to convergence. Then, CTF amplitude and phase corrections, finer angular sampling and solvent flattening via masking were performed for higher-resolution refinement. This process was iterated to convergence. According to the 0.5 Fourier shell

correlation criterion[41], the final resolution of the asymmetric reconstruction of HDL–CETP complex was 14 Å (**Supplementary Fig. 3**).

Three-dimensional reconstruction of CETP. The image processing is described in detail in **Supplementary Methods**.

Accession codes. Electron Microscopy Data Bank: the cryo-PS-EM density map of CETP and the NS-EM map of HDL–CETP are deposited under ID codes 5346 and 5347, respectively. Protein Data Bank: the previously published crystal structure for CETP is deposited under accession code 2OBD.

References

1. Barter, P.J. *et al.* Cholesteryl ester transfer protein: a novel target for raising HDL and inhibiting atherosclerosis. *Arterioscler. Thromb. Vasc. Biol.* **23**, 160–167 (2003).
2. Camejo, G., Waich, S., Quintero, G., Berrizbeitia, M.L. & Lalaguna, F. The affinity of low density lipoproteins for an arterial macromolecular complex. A study in ischemic heart disease and controls. *Atherosclerosis* **24**, 341–354 (1976).
3. Gordon, T., Castelli, W.P., Hjortland, M.C., Kannel, W.B. & Dawber, T.R. High density lipoprotein as a protective factor against coronary heart disease. The Framingham Study. *Am. J. Med.* **62**, 707–714 (1977).
4. Hayek, T. *et al.* Hypertriglyceridemia and cholesteryl ester transfer protein interact to dramatically alter high density lipoprotein levels, particle sizes, and metabolism. Studies in transgenic mice. *J. Clin. Invest.* **92**, 1143–1152 (1993).
5. Brown, M.L. *et al.* Molecular basis of lipid transfer protein deficiency in a family with increased high-density lipoproteins. *Nature* **342**, 448–451 (1989).
6. Inazu, A. *et al.* Increased high-density lipoprotein levels caused by a common cholesteryl-ester transfer protein gene mutation. *N. Engl. J. Med.* **323**, 1234–1238 (1990).
7. Niesor, E.J. Different effects of compounds decreasing cholesteryl ester transfer protein activity on lipoprotein metabolism. *Curr. Opin. Lipidol.* **22**, 288–295 (2011).
8. Miyares, M.A. Anacetrapib and dalcetrapib: two novel cholesteryl ester transfer protein inhibitors. *Ann. Pharmacother.* **45**, 84–94 (2011).
9. Kappelle, P.J., van Tol, A., Wolffenbuttel, B.H. & Dullaart, R.P. Cholesteryl ester transfer protein inhibition in cardiovascular risk management: ongoing trials will end the confusion. *Cardiovasc. Ther.* **29**, e89–e99 (2010).
10. Qiu, X. *et al.* Crystal structure of cholesteryl ester transfer protein reveals a long tunnel and four bound lipid molecules. *Nat. Struct. Mol. Biol.* **14**, 106–113 (2007).
11. Barter, P.J. & Jones, M.E. Kinetic studies of the transfer of esterified cholesterol between human plasma low and high density lipoproteins. *J. Lipid Res.* **21**, 238–249 (1980).
12. Ihm, J., Quinn, D.M., Busch, S.J., Chataing, B. & Harmony, J.A. Kinetics of plasma protein-catalyzed exchange of phosphatidylcholine and cholesteryl ester between plasma lipoproteins. *J. Lipid Res.* **23**, 1328–1341 (1982).
13. Tall, A.R. Plasma cholesteryl ester transfer protein. *J. Lipid Res.* **34**, 1255–1274 (1993).
14. Zhang, L. *et al.* Morphology and structure of lipoproteins revealed by an optimized negative-staining protocol of electron microscopy. *J. Lipid Res.* **52**, 175–184 (2011).
15. Chen, B. *et al.* Apolipoprotein AI tertiary structures determine stability and phospholipid-binding activity of discoidal high-density lipoprotein particles of different sizes. *Protein Sci.* **18**, 921–935 (2009).
16. Silva, R.A. *et al.* Structure of apolipoprotein A-I in spherical high density lipoproteins of different sizes. *Proc. Natl. Acad. Sci. USA* **105**, 12176–12181 (2008).
17. Zhang, L. *et al.* An optimized negative-staining protocol of electron microscopy for apoE4·POPC lipoprotein. *J. Lipid Res.* **51**, 1228–1236 (2010).
18. Ohi, M., Li, Y., Cheng, Y. & Walz, T. Negative staining and image classification - powerful tools in modern electron microscopy. *Biol. Proced. Online* **6**, 23–34 (2004).
19. Ren, G., Reddy, V.S., Cheng, A., Melnyk, P. & Mitra, A.K. Visualization of a water-selective pore by electron crystallography in vitreous ice. *Proc. Natl. Acad. Sci. USA* **98**, 1398–1403 (2001).
20. Ren, G., Cheng, A., Reddy, V., Melnyk, P. & Mitra, A.K. Three-dimensional fold of the human AQP1 water channel determined at 4 Å resolution by electron crystallography of two-dimensional crystals embedded in ice. *J. Mol. Biol.* **301**, 369–387 (2000).
21. Ren, G. *et al.* Model of human low-density lipoprotein and bound receptor based on CryoEM. *Proc. Natl. Acad. Sci. USA* **107**, 1059–1064 (2010).
22. Adrian, M., Dubochet, J., Fuller, S.D. & Harris, J.R. Cryo-negative staining. *Micron* **29**, 145–160 (1998).
23. Hayat, M.A. & Miller, S.E. *Negative Staining* (McGraw-Hill, 1990).
24. Morton, R.E. & Greene, D.J. The surface cholesteryl ester content of donor and acceptor particles regulates CETP: a liposome-based approach to assess the substrate properties of lipoproteins. *J. Lipid Res.* **44**, 1364–1372 (2003).
25. Swenson, T.L., Brocia, R.W. & Tall, A.R. Plasma cholesteryl ester transfer protein has binding sites for neutral lipids and phospholipids. *J. Biol. Chem.* **263**, 5150–5157 (1988).
26. Pettersen, E.F. *et al.* UCSF Chimera—a visualization system for exploratory research and analysis. *J. Comput. Chem.* **25**, 1605–1612 (2004).
27. Liu, J., Bartesaghi, A., Borgnia, M.J., Sapiro, G. & Subramaniam, S. Molecular architecture of native HIV-1 gp120 trimers. *Nature* **455**, 109–113 (2008).
28. Flemming, D., Thierbach, K., Stelter, P., Böttcher, B. & Hurt, E. Precise mapping of subunits in multiprotein complexes by a versatile electron microscopy label. *Nat. Struct. Mol. Biol.* **17**, 775–778 (2010).
29. Phillips, J.C. *et al.* Scalable molecular dynamics with NAMD. *J. Comput. Chem.* **26**, 1781–1802 (2005).
30. Atilgan, A.R. *et al.* Anisotropy of fluctuation dynamics of proteins with an elastic network model. *Biophys. J.* **80**, 505–515 (2001).
31. Doruker, P., Atilgan, A.R. & Bahar, I. Dynamics of proteins predicted by molecular dynamics simulations and analytical approaches: application to α-amylase inhibitor. *Proteins* **40**, 512–524 (2000).
32. Weers, P.M. & Ryan, R.O. Apolipophorin III: role model apolipoprotein. *Insect Biochem. Mol. Biol.* **36**, 231–240 (2006).
33. Saito, H. *et al.* Domain structure and lipid interaction in human apolipoproteins A-I and E, a general model. *J. Biol. Chem.* **278**, 23227–23232 (2003).
34. Mehta, R., Gantz, D.L. & Gursky, O. Human plasma high-density lipoproteins are stabilized by kinetic factors. *J. Mol. Biol.* **328**, 183–192 (2003).
35. Han, M. *et al.* Disruption of human plasma high-density lipoproteins by streptococcal serum opacity factor requires labile apolipoprotein A-I. *Biochemistry* **48**, 1481–1487 (2009).
36. Wang, S., Kussie, P., Deng, L. & Tall, A. Defective binding of neutral lipids by a carboxyl-terminal deletion mutant of cholesteryl ester transfer protein. Evidence for a carboxyl-terminal cholesteryl ester binding site essential for neutral lipid transfer activity. *J. Biol. Chem.* **270**, 612–618 (1995).
37. Grigorieff, N. FREALIGN: high-resolution refinement of single particle structures. *J. Struct. Biol.* **157**, 117–125 (2007).
38. Frank, J. *et al.* SPIDER and WEB: processing and visualization of images in 3D electron microscopy and related fields. *J. Struct. Biol.* **116**, 190–199 (1996).
39. Ludtke, S.J., Baldwin, P.R. & Chiu, W. EMAN: semiautomated software for high-resolution single-particle reconstructions. *J. Struct. Biol.* **128**, 82–97 (1999).
40. Galkin, V.E., Orlova, A., Cherepanova, O., Lebart, M.C. & Egelman, E.H. High-resolution cryo-EM structure of the F-actin-fimbrin/plastin ABD2 complex. *Proc. Natl. Acad. Sci. USA* **105**, 1494–1498 (2008).
41. Böttcher, B., Wynne, S.A. & Crowther, R.A. Determination of the fold of the core protein of hepatitis B virus by electron cryomicroscopy. *Nature* **386**, 88–91 (1997).

Author contributions

G.R., K.H.W. and X.Q. initiated and designed the project; X.Q. provided the soluble CETP; H.J.P. and R.M.K. contributed the LDL and VLDL; K.-A.R., M.O. and G.C. provided HDL; L.Z., F.Y. and G.R. collected the data; S.Z., D.L. and G.R. conducted the molecular simulation; G.R. solved the structure; G.R., L.Z., M.A.C. and X.Q. analyzed and interpreted the data; G.R. and S.Z. drafted the initial manuscript; M.A.C., H.J.P., K.H.W., K.-A.R., R.M.K., X.Q. and L.Z. discussed and revised the manuscript.

Competing financial interests

The authors declare no competing financial interests.

Additional information

Supplementary information is available online at http://www.nature.com/naturechemicalbiology/. Reprints and permissions information is available online at http://www.nature.com/reprints/index.html. Correspondence and requests for materials should be addressed to G.R.

SUPPLEMENTARY INFORMATION FOR

Structural basis of transfer between lipoproteins by cholesteryl ester transfer protein

Lei Zhang[1,2,3,11], Feng Yan[2,11], Shengli Zhang[3], Dongsheng Lei[3], M Arthur Charles[2], Giorgio Cavigiolio[4], Michael Oda[4], Ronald M Krauss[4], Karl H Weisgraber[5], Kerry-Anne Rye[6,7,8], Henry J Pownall[9], Xiayang Qiu[10] & Gang Ren[1,2,3*]

[1]Molecular Foundry, Lawrence Berkeley National Laboratory, Berkeley, CA 94720, USA. [2]School of Medicine, University of California, San Francisco, CA 94158, USA. [3]Department of Applied Physics, Xi'an Jiaotong University, Xi'an 710049, China. [4]Children's Hospital Oakland Research Institute, Oakland, CA 94609, USA. [5]Gladstone Institute of Neurological Disease, University of California, San Francisco, CA 94158, USA. [6]Lipid Research Group, The Heart Research Institute, Sydney, NSW, 2050, Australia. [7]Faculty of Medicine, University of Sydney, NSW, 2060, Australia. [8]Department of Medicine, University of Melbourne, Victoria 3010, Australia. [9]Department of Medicine, Baylor College of Medicine, Houston, TX 77030, USA. [10]Pfizer Inc, Groton, CT 06430, USA. [11]These authors contributed equally to this work. [*]e-mail: gren@lbl.gov

Supplementary Information:

SUPPLEMENTARY METHODS

Protein isolation and purification. Recombinant human CETP (~53 kDa before post-translational modifications) from the Qiu laboratory was expressed and purified from the dihydrofolate reductase–deficient Chinese hamster ovary cell line DG44[1]. The CETP concentration was determined by absorbance assay (280 nm). Discoidal reconstituted HDL (rHDL) consisting of apoA-I purified from pooled samples of normal human plasma, l-palmitoyl-2-oleoyl phosphatidylcholine (POPC), and unesterified cholesterol (UC) (initial POPC:UC:apoA-I molar ratio was 100:10:1) was prepared by the cholate dialysis method[2]. Discoidal HDL particles were converted into spherical rHDL by incubation with fatty acid–free bovine serum albumin, β-mercaptoethanol, ultracentrifugally isolated LDL and purified lecithin:cholesterol acyltransferase (LCAT)[3]. The spherical HDL species were isolated in the Rye laboratory by sequential ultracentrifugation in the $1.07 < d < 1.21$ g/ml density range as previously described[3]. The apoA-I concentration in the spherical HDL preparations was determined on a Hitachi 902 automatic analyzer (Roche Diagnostics, GmbH, Mannheim, Germany) by the bicinchoninic assay using BSA as a standard [4]. LDL (d = 1.006–1.069 g/ml), and VLDL (d < 1.006 g/ml) were isolated in the Pownall and Krauss laboratories respectively by sequential flotation of plasma from fasted, healthy male volunteers, and further purified by isopycnic density gradient ultracentrifugation as previously described[5]. The protein concentrations of the LDL and VLDL were determined by an absorbance assay (280 nm). The polycolonial CETP antibodies, H300 and N13, were purchased from Santa Cruz Biotechnology, Inc., CA.

Binary complex formation. To prepare the CETP–HDL complexes, CETP (final concentration 0.93 mg/ml [17.5 μM]) and HDL (final apoA-I concentration from 2.96 mg/ml [35 μM], to 0.30 mg/ml [3.5 μM]) were incubated at 37°C for 2D NS-EM, or at 4°C for 3D reconstructions for 1 hour at molar ratios ranging from 0.5:1 to 5:1 (CETP:HDL, assuming three apoA-I molecules/HDL particle). CETP–LDL and CETP–VLDL complexes were formed similarly using CETP (final concentration 0.6 mg/ml for LDL and 0.23 mg/ml for VLDL), LDL (final apoB-100 concentration 3.1 mg/ml [5.6 μM]), and VLDL (final protein concentration 1.3 mg/ml [2.1 μM]) at molar ratios of 2:1 (CETP:LDL) and 2:1 (CETP:VLDL), respectively. Although the apolipoprotein content of VLDL varies, VLDL contains one apo B-100 molecule, which is ~550 kDa and significantly larger than other the apolipoproteins in these particles (E: 35 kDa, A-I: 28 kDa, C-I, II, III: < 10 kDa). Thus, a reasonable estimation of the molecular mass of proteins contained in VLDL is ~600 kDa for the calculation of VLDL molarities. All samples were prepared by optimized negative-staining (OpNS) and then examined and imaged with either a FEI Tecnai T20 (Philips Electron Optics/FEI, Eindhoven, The Netherlands) or a Zeiss Libra 120 transmission electron microscope with 20ev energy filter (Carl Zeiss NTS GmbH, Germany).

Ternary complex formation. CETP (final concentration 0.33 mg/m [6.2 μM]) was incubated for 30 minutes at 37°C or 4°C, as described above for binary complexes, with HDL (final apoA-I concentration 0.26 mg/ml [3.1 μM]) at a molar ratio of 2:1 (CETP:HDL), and LDL (final apoB-100 concentration 0.86 mg/ml [1.6 μM]) was added at a molar ratio of 2:1 (HDL:LDL). HDL–CETP–VLDL complexes were prepared with VLDL (final protein concentration 0.93 mg/ml, [1.6 μM]) and the HDL–CETP complex at a molar ratio of 2:1 (HDL:VLDL).

Assessment of CETP function by EM. HDL/CETP/LDL mixtures were prepared by combining CETP (final concentration 0.33 mg/ml), HDL (final apoA-I concentration 0.26 mg/ml), and LDL (final apoB-100 concentration 0.86 mg/ml) at a molar ratio of 4:2:1 (CETP:HDL:LDL) at 4°C, then incubating them at 37°C for up to 48 hours in a thermo-incubator. Each aliquot was diluted to an apoA-I concentration of 0.005 mg/ml with DPBS buffer, and prepared as NS-EM specimens with 1% (w/v) uranyl formate (UF)[6,7]. Samples of HDL/CETP, LDL/CETP, HDL/LDL, HDL, LDL, HDL/CETP/LDL/H300, and HDL/CETP/LDL/N13 were prepared similarly, with a molar ratio of antibody (H300/N13) to CETP of 2:1.

Labeling lipoprotein–CETP complexes with antibodies. HDL (final apoA-I concentration 0.26 mg/ml) or LDL (final apoB-100 concentration 0.86 mg/ml) were incubated at 4°C for 0.05– 4 hours with two molar equivalents of CETP (final concentration 0.33 mg/ml) and then at 4°C overnight with the anti-CETP antibodies N13 or H300 (final concentration 1.86 mg/ml) at a molar ratio of 1:2 (CETP:antibody). The sample was diluted so that the CETP concentration was 0.002 mg/ml and prepared for NS-EM specimens within 5 minutes.

Statistical analysis. For statistical analyses of the HDL–CETP–LDL ternary complexes, all LDL particles in each micrograph were windowed and identified using *boxer* in the EMAN software package[8]. A total of 5 micrographs were used. Before particle selection, the contrast transfer function (CTF) of each micrograph was determined and then phase corrected by the phase-flip option in *ctfit* (EMAN software). Ternary complexes were first Gaussian low-pass filtered before being identified and selected by examining the particles at 4× zoom. The criteria to distinguish ternary complexes were as follows: 1) the shortest distance between the surfaces of the LDL and HDL particles should be shorter than longest dimension of CETP, i.e. <130 Å; and 2) there should be an identifiable small connecting density between the HDL and LDL particles. 523 LDL particles were selected from 5 micrographs, in which 130 (~25%) particles satisfied these criteria. A HDL particle may be randomly distributed around the LDL particle it is bridged to, resulting in the connecting portion being obscured from view. Thus it is reasonable to believe that the actual percentage of LDL particles belonging to a ternary complex is higher than the observed ~25%. For the statistical analysis of the HDL–CETP–VLDL ternary complexes, a percentage of ~30% for VLDL particles belonging to a ternary complex was obtained by following a protocol similar to that of HDL–CETP–LDL complexes.

For statistical analysis of particle size in the functional assays, a total of ~500 HDL and/or LDL particles from each of the various incubation protocols were manually selected from CTF-corrected micrographs as described above. Particle size was determined by measuring diameters along two orthogonal directions, one of which was the longest dimension. The geometric averages of two diameters were calculated and expressed as mean ± standard deviation (SD). The Python program was used for data analysis. The absorbance histograms for the pixels in each image were scaled to the mean, and the SD was used as error. To get a clear comparison between various incubation conditions, mean size and SD values were divided by the initial mean size, i.e., the mean size at 3 minutes.

Molecular dynamics analysis by NAMD. To examine structural fluctuations, the crystal structure of CETP (PDB code 2OBD[1]) in a cubic box was solvated with 67,452 TIP3P water molecules with the VMD Solvate plug-in[9]. The box was extended 25 Å from the protein. To neutralize the system and obtain a physiological salt concentration (0.15 M NaCl), 199 Na$^+$ and 182 Cl$^-$ ions were added. The final model system contained ~211,000 atoms. To reduce steric contacts, 10,000 energy minimization steps were applied. All simulations were carried out using NAMD[10] with force fields of CHARMM22[11], CHARMM27[12], and from the literature[13]. Periodic boundary conditions and a 12 Å cutoff for Van der Waals interactions were applied. The long-range electrostatic interactions were treated using the Particle-Mesh Ewald (PME) method[14]. The system was heated from 0 K to 310 K in steps of 10 K in a 2 ps time period. Then 8 ns MD simulation was performed at 310 K and 1 atm. The first 2 ns were considered equilibration, and root mean square fluctuations (RMSFs) were calculated over the last 6 ns after all the trajectories were aligned with their averaged structure. Langevin dynamics and Langevin piston Nose-Hoover methods[15] were used to keep temperature and pressure constant. Further, to ensure the reliability of simulation results, three total simulations were carried out independently. The averaged RMSFs were obtained from these three independent molecular dynamics simulations and used for analysis of molecular fluctuation.

Molecular dynamics analysis by ANM. An alternative analysis of the large-scale molecular dynamics motion is the anisotropic network model (ANM)[16], which is a simple normal-mode analysis (NMA) tool for assessing vibrational motions in molecular systems. The crystal structure of CETP (PDB code 2OBD[1]) was used to analyze the residue level for prediction of anisotropic motions by elastic network (EN) methods. The orientation of each interaction with respect to the global coordinate system was considered within ~20 types of the forces-constant matrix to predict and explore the large-scale fluctuations and dynamic regions in CETP structure. According to this analysis, both ends of these β-barrel domains are flexible. Torsional analysis along the CETP channel direction (mode 3) suggested that both ends of β-barrel domains are rich in residues with a high B-factor (>130), such as E46-A48, G53-K56, G100-S112, S146-K149, Q155-E157, T168-F170, M288-A294, E297-Q305, G314-Q318, P351-H357, and L397-E399. Remarkably, the N-terminal β-barrel can be twisted to ~15° under a vibrational amplitude scaling of 1. The "open" conformation was generated initially by ANM under the torsional vibration model (mode 3), then VMD and NAMD were used to recover the side chains associated with energy minimization for reducing the steric contacts in a cubic water box.

3D reconstruction of CETP. To avoid bias in the initial model for CETP reconstruction, we used a featureless solid cylinder as an initial starting model. The cylinder was 125 Å long and 30 Å in diameter, typical of the structural features displayed in the reference-free class averages. The 3D reconstruction was constructed from 8,879 windowed particles from cryo-PS-EM images after CTF correction and by following a protocol similar to that of HDL–CETP complex reconstruction for iteration and convergence. According to the 0.5 Fourier shell correlation criterion, the final resolution of the asymmetric reconstruction for CETP was 13Å (**Supplementary Fig. 3**).

SUPPLEMENTARY RESULTS

CETP reaction mechanism.
CETP with HDL and/or LDL were incubated at physiological temperatures for up to 48 hours during which HDL size was measured using the OpNS-EM. When only two of three components (CETP, HDL and LDL) were incubated for up to 4 hours, HDL size did not change (**Fig. 5** and **Supplementary Fig.12a**). However, when all three components were co-incubated, ternary complexes were observed at all incubation times (**Supplementary Fig.12b**), during which the mean HDL particle size decreased by 25.8 ± 8.0% after 4 hours (black circles in **Fig. 5**, **Supplementary Table 1**). This decrease suggests that the HDL particles are depleted of core lipids by CETP (i.e., there is a net mass transfer of CEs to LDL). The rate constant for CE transfer was 0.58 ± 0.19 h^{-1} ($r^2>0.94$) based on HDL size changes and the assumption that the decrease in HDL size resulted only from CE outflow[17]. In contrast, the size of the LDL particles did not change noticeably, most likely because the amount of accepted CE is small relative to the LDL particle volume, which is ~30 times greater than that of HDL. These data suggest that CETP transfers core lipids from HDL to LDL and possibly VLDL, as ternary complexes. These experiments do not support the shuttle mechanism in which CETP dissociates from the HDL surface after it has removed the maximum amount of CE from the HDL core, i.e., after 3-4 hours of incubation. Specifically, with the shuttle mechanism, the percentage of HDL–CETP complexes should decrease over time after incubation of CETP with HDL, something that was not observed even after 48 hours.

We performed additional experiments using CETP polyclonal antibodies H300 and N13. The epitopes for H300 are near the C-terminal end of CETP while those for N13 are near the N-terminal β-barrel domain close to the central β-sheet. The antibodies were incubated separately with HDL, CETP and LDL at 37°C, and aliquots were collected at various times and examined by the OpNS-EM method. Co-incubation of H300 with LDL and HDL inhibited the decrease in the size of HDL (**Fig. 5** and **Supplementary Table 1**), from which we conclude that H300 inhibits CE transfer. In contrast, a similar incubation in which H300 was replaced by N13 reduced HDL size ~18.4% after 2 hours, a value similar to that observed without antibodies (**Fig. 5** and **Supplementary Table 1**).

EM images utilizing polyclonal antibodies, which recognize multiple epitopes, can be misleading because there could be as many complexes as epitopes. However, measurements of HDL size change are less ambiguous because they reveal the predominant class of epitopes blocked by the array of antibodies. Thus, H300 binds near the CETP C-terminus and in so doing blocks formation of the ternary (HDL–CETP–LDL) and binary (LDL–CETP) complexes and inhibits HDL to LDL CE transfer. Given that our data implicates the N- and C-terminal regions of CETP with lipoproteins, the absence of inhibition by the N-13 antibody, which binds nearer to the central region of CETP on the N-terminal side of CETP, is not expected to be inhibitory, as observed.

Although the above results do not favor the shuttle mechanism for CETP-mediated transfer of neutral lipids between HDL and LDL, they do not exclude the possibility that CETP shuttles neutral lipids between HDL particles themselves. Although the mean HDL particle size did not change after incubation with CETP for up to 2 hours, the standard deviation at 2 hours was larger
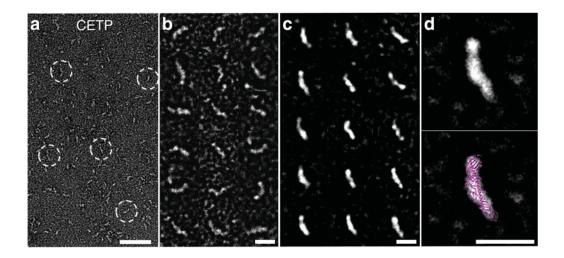
than that at 3 minutes (**Supplementary Table 1**). The micrographs and histograms show small amounts (<5%) of larger HDL particles (>200 Å), while the remaining HDL particles are smaller in size, raising the possibility that CETP may shuttle CE among HDL particles.
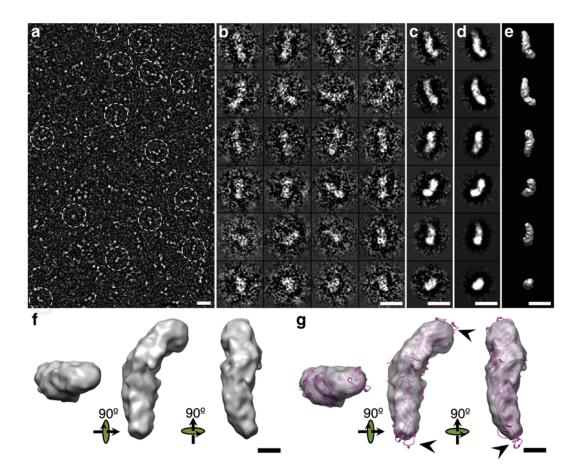
Supplementary Table

Supplementary Table 1. HDL size changes during CETP incubations with lipoproteins and antibodies

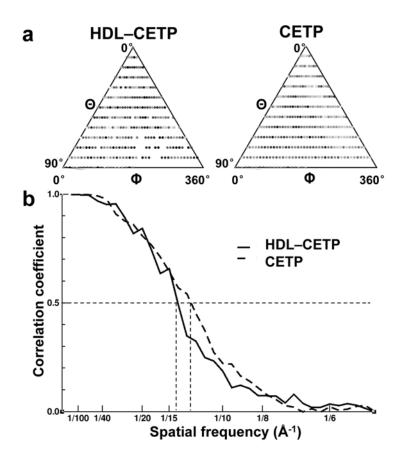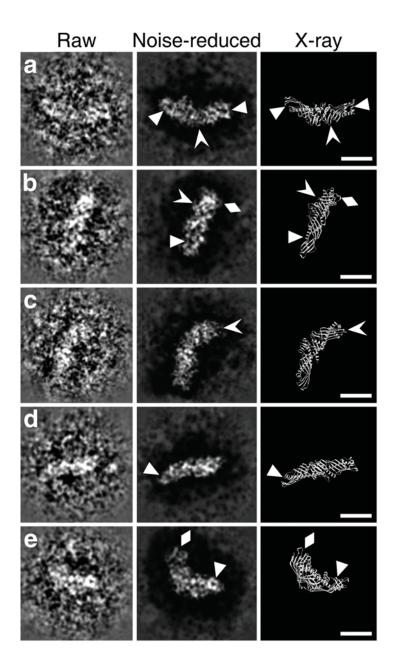| Incubation time	-CETP						+CETP					
	HDL/LDL		HDL/CETP		HDL alone		HDL/CETP/LDL		HDL/CETP/LDL/H300		HDL/CETP/LDL/N13	
	Diameter (%)	SD	Diameter (%)	SD	Diameter (%)	SD	Diameter (%)	SD	Diameter (%)	SD	Diameter (%)	SD
3 mins	100.00	7.61	100.00	8.74	100.00	12.48	100.00	13.60	100.00	8.19	100.00	7.90
20 mins	101.38	8.34	99.30	13.14	97.04	13.80	92.19	13.38	103.01	8.40	88.65	9.46
1 hour	98.85	7.87	92.32	17.00	98.44	13.85	82.28	14.53	94.97	10.34	87.14	9.33
2 hours	95.77	13.14	93.07	23.84	94.86	13.40	74.95	11.00	97.57	10.94	81.63	7.73
4 hours	97.80	7.10	87.44	21.59	104.23	11.67	74.22	7.97	87.20	9.42	77.83	9.87

Supplementary Figures

Supplementary Figure 1 | OpNS-EM images of CETP. (**a**) Survey view of the micrograph shows the banana-shaped CETP (dashed circles). (**b**) Selected particles of CETP are ~125 Å long and ~30 Å wide. (**c**) In these randomly oriented particles selected, reference-free, and class-averaged images usually show one distal end of CETP larger and denser than the other, corresponding to the C- and N-terminal β-barrel domains, respectively. (**d**) A reference-free, class average image demonstrating a larger, dense and more globular end and a smaller, less dense and more tapered end (top panel). Overlaying the CETP crystal structure (purple) onto this class average image shows a near-perfect match in structural shape and size (bottom panel). Scale bars: **a**, 500 Å; **b-d**, 100 Å.
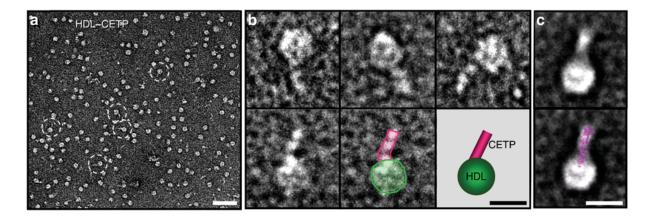
Supplementary Figure 2 | 3D reconstruction of CETP by cryo-PS-EM. (**a**) Survey view (reversed contrast) of CETP molecule alone (dashed circles). (**b**) 24 representative views of selected and windowed raw particles of CETP and (**c**) their class averages are compared with (**d**) corresponding views of the 3D reconstruction projections and (**e**) 3D reconstruction of the same views. (**f**) The 3D density map of CETP (~13 Å resolution) reconstructed from 8,879 CETP particle images shows a banana shape. (**g**) The crystal structure of CETP (purple) inserted into the EM density map demonstrates a near-perfect match to the density map in shape and size, except for the distal portions of the N- and C-terminal β-barrel domains, segments of which protrude (arrows) from the density envelope. Scale bars: **a-e**, 100 Å; **f** and **g**, 20 Å.
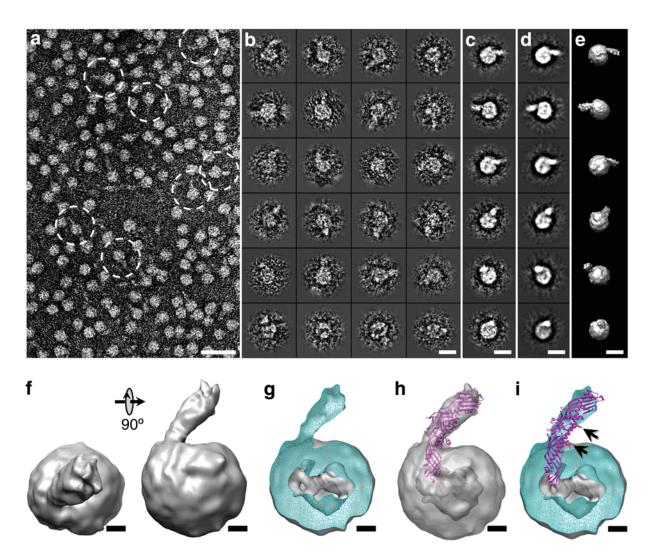
Supplementary Figure 3 | Analysis of single-particle image reconstruction of CETP and HDL–CETP complexes. (**a**) Histogram of the raw images in each view of the final model. All views of the HDL–CETP complex (left) and CETP alone (right) are well represented, and there are no obvious preferential orientations. Images were aligned translational (x and y) and rotationally in-plane (ω), and each particle was assigned to the group to which it correlated best. Each dot represents a projection of the final model for a given Θ and Φ value. (**b**) Fourier shell correlation to determine map resolution. The total data set of images was divided into two equal groups, the particles in each data set were aligned independently with projections of the final model, and two independent maps were correlated in Fourier space. The curves cross the 0.5 threshold at ~14 Å and ~13 Å resolution for the HDL–CETP complex and the CETP-only 3D reconstructions respectively.
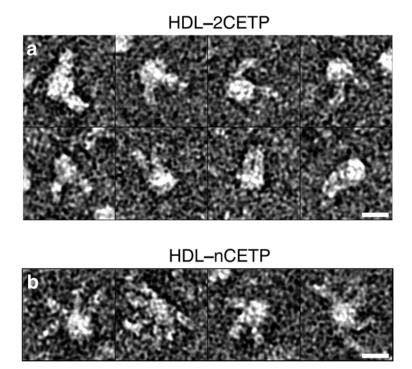
Supplementary Figure 4 | High-resolution CETP images by cryo-PS-EM. Five selected high-resolution and raw particle images of CETP (contrast reversed, left column **a**-**e**) were manually noise-reduced around the raw particle images' edges for easy-visualization (middle column **a**-**e**). The latter images can be compared with the crystal structure's main chain at a similar orientation (right column **a**-**e**). The high-resolution, raw image areas display detailed structural features of CETP. For example, these particles have very similar features to the crystal structure, e.g., the small, circular holes near both distal ends can be visualized in the noise-reduced images (triangles in rows **a**, **b**, **d** and **e**); further, the striations in the C-terminal domains of the images match the β-sheets of the crystal structure (arrows in rows **a**, **b** and **c**) and finally, loops protruding from the C-terminal end of the CETP images are similar to the crystal structure (diamonds in rows **b** and **e**). Scale bars, 50 Å.
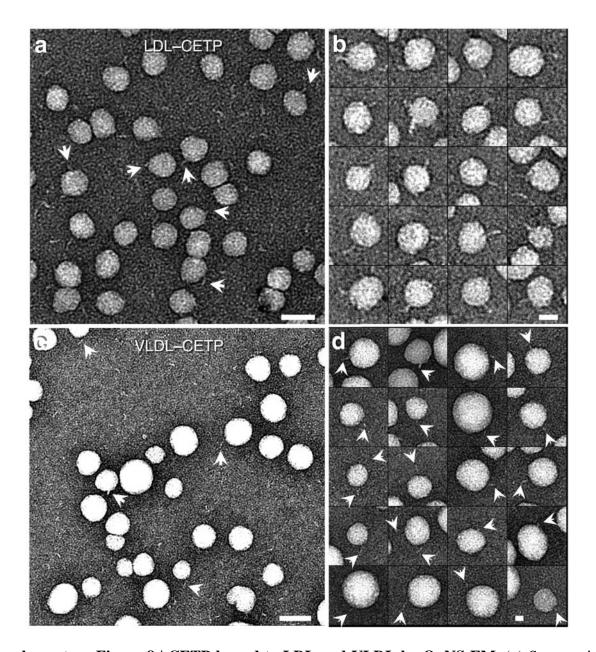
Supplementary Figure 5 | HDL–CETP complexes imaged by OpNS-EM. (**a**) Survey view of the HDL–CETP complexes (dashed circles) shows single CETP particles bound to single HDL particles to form binary complexes. (**b**) Selected binary complexes of CETP and HDL show the banana-shaped CETP interacting with the round-shaped HDL. (**c**, upper panel) A selected, reference-free and class-averaged image demonstrates a linear-shaped density connected to a rounded particle forming the HDL–CETP complex. Overlaying the CETP crystal structure onto this linear portion of the complex shows a near-perfect match in shape and size (**c**, lower panel). The length of CETP extending from the surface of HDL is 77±10 Å, which suggests the β-barrel domain penetrates the HDL surface monolayer to a depth of ~48 Å. Scale bars: **a**, 500 Å; **b-c**, 100 Å.

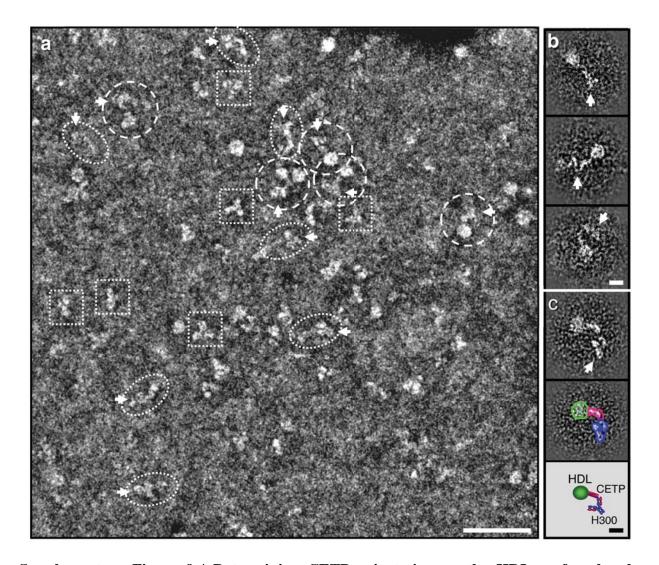**Supplementary Figure 6 | 3D reconstruction of HDL–CETP complex by OpNS-EM. (a)** Survey view of the negative-stained EM structure of HDL–CETP complexes (white circles). (**b**) 24 representative views of selected and windowed, individual raw particles of HDL–CETP complexes, and (**c**) their class averages are compared with (**d**) the same view of the reconstructed projections and (**e**) the 3D density map. (**f**) The 3D density map (~14 Å resolution, reconstructed from 6,607 homogenous particle images) shows a binary complex in which the banana-shaped CETP is attached to the HDL surface at a ~45° angle. (**g**) Cut-away surface view (cyan) shows the HDL portion containing a high-density outer shell (~18–27 Å thick) and a low-density cavity (~55 Å in diameter). Inserting the CETP crystal structure into the EM density map of a HDL–CETP complex shows the N-terminal β-barrel domain of CETP penetrating the outer shell of HDL and its distal end in the low-density core in transparency (**h**) and cut-away surface view (**i**). The black arrows in (**i**) point to two PL-binding pores, one of which is adjacent (~15 Å) to the HDL surface while the other is further away, indicating that the phospholipid-binding pores of CETP do not interact directly with the HDL core. Scale bars: **a**, 200 Å; **b-e**, 100 Å; **f-i**, 20 Å.
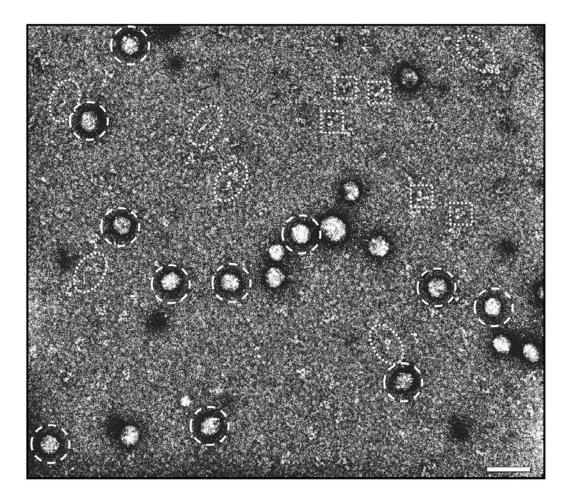
HDL–2CETP

HDL–nCETP

Supplementary Figure 7 | Multiple CETPs penetrate to one HDL particle by OpNS-EM. (a) Selected complexes of HDL–CETP showing two CETP molecules interacting with one HDL particle. (**b**) A minor population of complexes shows 3 or more CETP molecules attached to one HDL particle. Scale bars, 100 Å.
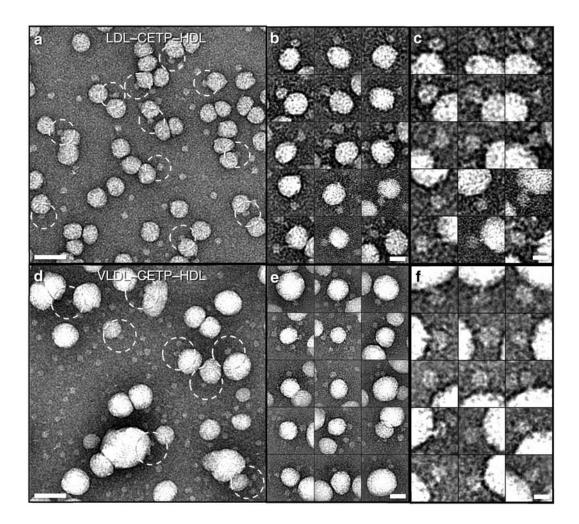
Supplementary Figure 8 | CETP bound to LDL and VLDL by OpNS-EM. (**a**) Survey view of the LDL–CETP complexes shows single CETP particles (arrow) bound to single LDL particles. (**b**) Selected binary complexes of CETP and LDL show that the distal end of the linear or banana-shaped CETP interacts with the round-shaped LDL. (**c**) Survey view and (**d**) selected complexes show that some VLDL particles have one or more linear-shaped CETP on the surface (arrows).
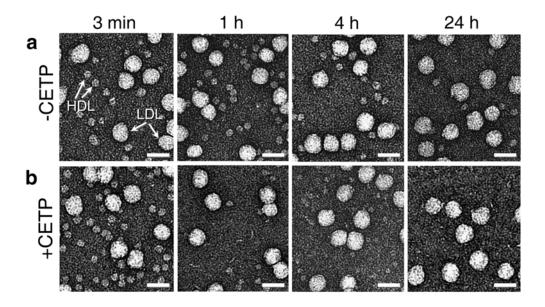
Supplementary Figure 9 | Determining CETP orientation on the HDL surface by the immuno-EM. CETP antibody, H300, is used as a landmark for CETP. (**a**) Survey view of a sample from incubation with H300, CETP and HDL together. The micrograph shows the "Y"-shaped antibody H300 alone (dotted squares), CETP–H300 complexes (dotted ovals) and HDL–CETP–H300 complexes (dashed circles). (**b** & **c**) Selected HDL–CETP–H300 complexes show antibody is located at the distal, free end of CETP. H300 indicated by arrows. Scale bars: **a**, 500 Å; **b** and **c**, 100 Å.
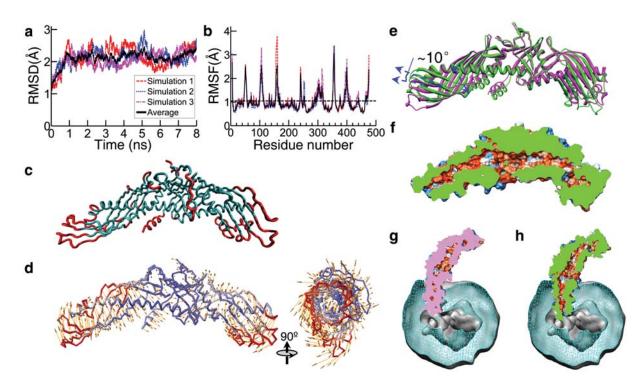
Supplementary Figure 10 | Determining CETP orientation on the LDL surface by the immuno-EM. LDL was incubated with CETP and H300. Survey view of the sample shows the round- shaped LDL (dashed circles), "Y"-shaped antibody H300 (dotted squares), and CETP–H300 complexes (dotted ovals); however, LDL–CETP–H300 complexes are rarely observed. Scale bar, 500 Å.

Supplementary Figure 11 | CETP forms ternary complexes by OpNS-EM. (**a**) Survey view shows LDL and HDL particles immediately adjacent to each other with occasional bridge-like CETP structures observed (dashed circles). (**b**) Selected ternary complexes of CETP, HDL, and LDL show that both distal ends of the bridging CETP interact with each lipoprotein, and their corresponding higher power views are shown in (**c**). Using VLDL instead of LDL, survey view images of selected complexes (**d**), selected VLDL and HDL particles (**e**) and their corresponding higher power views (**f**) show CETP bridging HDL and VLDL. Scale bars: **a** and **d**, 500 Å; **b** and **e**, 300 Å; **c** and **f**, 100 Å.

Supplementary Figure 12 | Analysis of HDL size change during incubation with CETP.
Samples were collected and viewed by OpNS-EM. (**a**) When HDL is incubated with LDL, but
without CETP, the HDL particle size remains unchanged up to 4 hours. (**b**) When HDL is
incubated with CETP and LDL, the HDL particle size decreases after 1 hour of incubation. Scale
bars, 300 Å.

Supplementary Figure 13 | Molecular dynamics simulation of CETP crystal structure. By the NAMD simulation method, (**a**) the equilibration of the system was monitored through root mean square deviations (RMSDs). (**b**) After equilibration, CETP mobility is evaluated by calculating root mean square fluctuations (RMSFs). (**c**) The regions with the greatest fluctuations (top 30%) are near the distal ends (left-side, N-terminus; right-side, C-terminus) of the CETP β-barrel domains and the α-helix X (red). (**d**) By torsion analysis of the anisotropic network model (ANM), the vibrational motion of CETP shows the structure is torsionally flexible along its long axis. The most flexible portions are near the distal ends of the β-barrel domains (red). (**e**) Structural models of CETP before and after twisting using ANM. The torsion analysis along the CETP channel direction (mode 3) shows that the N-terminal β-barrel distal end can open a pore with only ~15° of twisting. Superimposing the structures together before twisting ("closed-state", magenta) and after twisting ("open-state", green), the ribbon diagram shows the N-terminal β-barrel domain enlargement (blue arrows, ~5 Å), causing the β-strands to become slightly vertical or perpendicular to the tunnel axis (~10° of tilting). (**f**) The cut-away surface of CETP in the "open-state" shows the isolated, hydrophobic cavities of the "close-state" connected together forming a continuous, hydrophobic channel along its long axis. (**g**) Superimposing CETP in the "closed-state" and (**h**) the "open-state" onto the HDL–CETP density map, the cut-away surface views show that the "opened" N-terminal β -barrel pore penetrates into the central CE core of HDL.

Supplementary References

1. Qiu, X. et al. Crystal structure of cholesteryl ester transfer protein reveals a long tunnel and four bound lipid molecules. *Nat. Struct. Mol. Biol.* **14**, 106-13 (2007).
2. Cavigiolio, G. et al. The interplay between size, morphology, stability, and functionality of high-density lipoprotein subclasses. *Biochemistry* **47**, 4770-9 (2008).
3. Rye, K.A. & Barter, P.J. The influence of apolipoproteins on the structure and function of spheroidal, reconstituted high density lipoproteins. *J. Biol. Chem.* **269**, 10298-303 (1994).
4. Smith, P.K. et al. Measurement of protein using bicinchoninic acid. *Anal Biochem* **150**, 76-85 (1985).
5. Gaubatz, J.W. et al. Dynamics of dense electronegative low density lipoproteins and their preferential association with lipoprotein phospholipase A(2). *J. Lipid Res.* **48**, 348-57 (2007).
6. Zhang, L. et al. Morphology and structure of lipoproteins revealed by an optimized negative-staining protocol of electron microscopy. *J. Lipid Res.* **52**, 175-84 (2011).
7. Zhang, L. et al. An optimized negative-staining protocol of electron microscopy for apoE4 POPC lipoprotein. *J. Lipid Res.* **51**, 1228-36 (2010).
8. Ludtke, S.J., Baldwin, P.R. & Chiu, W. EMAN: semiautomated software for high-resolution single-particle reconstructions. *J. Struct. Biol.* **128**, 82-97 (1999).
9. Humphrey, W., Dalke, A. & Schulten, K. VMD: visual molecular dynamics. *J. Mol. Graph.* **14**, 33-8, 27-8 (1996).
10. Phillips, J.C. et al. Scalable molecular dynamics with NAMD. *J. Comput. Chem.* **26**, 1781-802 (2005).
11. MacKerell, A.D. et al. All-atom empirical potential for molecular modeling and dynamics studies of proteins. *J. Phys. Chem. B* **102**, 3586-3616 (1998).
12. Feller, S.E. & MacKerell, A.D. An improved empirical potential energy function for molecular simulations of phospholipids. *J. Phys. Chem. B* **104**, 7510-7515 (2000).
13. Pitman, M.C., Suits, F., Mackerell, A.D., Jr. & Feller, S.E. Molecular-level organization of saturated and polyunsaturated fatty acids in a phosphatidylcholine bilayer containing cholesterol. *Biochemistry* **43**, 15318-28 (2004).
14. Darden, T., D. York, L. Pedersen. Particle mesh Ewald: An N log (N) method for Ewald sums in large systems. *J. Chem. Phys.* **98**(1993).
15. Feller, S.E., Zhang, Y.H., Pastor, R.W. & Brooks, B.R. Constant-Pressure Molecular-Dynamics Simulation - the Langevin Piston Method. *J. Chem. Phys.* **103**, 4613-4621 (1995).
16. Doruker, P., Atilgan, A.R. & Bahar, I. Dynamics of proteins predicted by molecular dynamics simulations and analytical approaches: application to alpha-amylase inhibitor. *Proteins* **40**, 512-24 (2000).
17. Han, M. et al. Disruption of human plasma high-density lipoproteins by streptococcal serum opacity factor requires labile apolipoprotein A-I. *Biochemistry* **48**, 1481-7 (2009).